PAPER

Check for updates

Interfacial chemistry governs SERS detectability of trimethoprim and ketoprofen: adsorption geometry and chloride-mediated activation

Dao Thi Nguyet Nga, [ID] † Ha Anh Nguyen, [ID] †* Mai Quan Doan [ID] and Anh-Tuan Le [ID] *

Pharmaceutical residues such as trimethoprim (TMP) and ketoprofen (KTP) are of growing environmental concern due to their persistence in wastewater and potential ecological impacts. In this study, we developed and evaluated electrochemically synthesized silver nanoparticles (e-AgNPs) immobilized on aluminum substrates as surface-enhanced Raman scattering (SERS) sensors for the detection of TMP and KTP. Structural and morphological characterization confirmed uniform, crystalline nanoparticles with an optimal size (~50 nm) for plasmonic enhancement. Electrochemical measurements showed that TMP and KTP possess nearly identical LUMO levels, yet their SERS responses differed markedly. TMP exhibited strong and reproducible SERS bands, enabling direct quantitative detection over a wide linear range (10^{-4} M to 10^{-8} M) with a detection limit of 3.84×10^{-9} M. In contrast, KTP showed intrinsically weak signals due to unfavorable adsorption geometry. Chloride modification (10^{-4} M NaCl) effectively "activated" KTP detectability by displacing citrate ligands and forming $Ag-Cl_x^-$ surface states, which facilitated the adsorption and charge transfer of the substrate. Under optimized conditions, KTP was quantified over 10^{-4} M to 10^{-7} M with a detection limit of 2.69×10^{-8} M. Real-sample validation demonstrated reliable recoveries of TMP (89–96%) and KTP (88–95%) in spiked tap water and commercial pharmaceutical tablets, despite matrix interferences. These obtained results highlight the decisive role of adsorption chemistry in SERS detectability and demonstrate that interfacial modification with chloride can extend SERS applicability to weakly adsorbing pharmaceutical pollutants, offering a sensitive platform for environmental monitoring and pharmaceutical quality control.

1. Introduction

Pharmaceutical residues are now recognized as contaminants of emerging concern, often persisting through conventional wastewater treatment and accumulating in rivers, lakes, and even groundwater. These residues endanger not only ecosystems but also human health *via* drinking water and food chains. Two pharmaceuticals, ketoprofen (KTP) and trimethoprim (TMP), are representative examples of this risk.

KTP, a non-steroidal anti-inflammatory drug (NSAID), has been detected in wastewater effluents and receiving rivers at concentrations ranging from 3.15 ng L^{-1} to 209 μg L^{-1}, reflecting both low background levels and episodic spikes in polluted systems.[1] Even at trace levels, KTP has demonstrated developmental and physiological toxicity in freshwater species such as algae and fish.[2]

TMP, a bacteriostatic antibiotic frequently prescribed in combination with sulfamethoxazole, is consistently reported in wastewater treatment plant (WWTP) influents and effluents at 0.41–1.0 μg L^{-1},[3] and in rivers at tens to hundreds of ng L^{-1}, occasionally up to 0.02–0.04 μg L^{-1} in UK and Japanese waters.[4] Its persistence in wastewaters has been widely documented.[5] At environmentally relevant concentrations, TMP inhibits algal growth and alters microbial community functions,[6] while even 10–100 μg L^{-1} is sufficient to exert selective pressure favoring resistant *Escherichia coli* strains,[7] thereby contributing to the global crisis of antimicrobial resistance (AMR). Wastewater and urban runoff are now recognized as critical hotspots for the dissemination of AMR genes, further underscoring the need for sensitive monitoring tools.[8,9]

Analytical monitoring of such pharmaceutical residues remains challenging. Conventional approaches, particularly high-performance liquid chromatography (HPLC) and liquid chromatography–mass spectrometry (LC–MS), provide excellent sensitivity and specificity. However, they are expensive, require skilled operators, involve time-consuming sample preparation, and are often limited to centralized laboratories. These drawbacks hinder large-scale or field-based surveillance.[10–12]

Phenikaa University Nano Institute (PHENA), Phenikaa School of Engineering (PSE), Phenikaa University, Hanoi, 12116, Vietnam. E-mail: anh.nguyenha@phenikaa-uni.edu.vn; tuan.leanh@phenikaa-uni.edu.vn

† D. T. N. Nga and H. A. Nguyen contributed equally to this work.

Surface-enhanced Raman scattering (SERS) has attracted growing attention as a complementary technique for pharmaceutical detection. By coupling the molecular vibrational specificity of Raman spectroscopy with electromagnetic amplification from localized surface plasmon resonance in metallic nanostructures, SERS can provide enhancement factors of 10^6–10^8. This enables detection of trace analytes, even at single-molecule levels, within complex matrices.[13–15] Importantly, SERS enhancements arise not only from electromagnetic "hot spots" (electromagnetic mechanism – EM) but also from chemical mechanism (CM), particularly charge-transfer (CT) interactions between the analyte and the metal substrate.[14,16,17] These CT processes depend on the relative energies of the analyte frontier molecular orbitals and the metal Fermi level, underscoring the need to consider electronic alignment as well as adsorption geometry when evaluating SERS performance.[18,19]

In our previous work, we experimentally demonstrated the decisive role of the lowest unoccupied molecular orbital (LUMO) in enabling SERS enhancement.[20] Using chloramphenicol and amoxicillin as model analytes, we showed that antibiotics with LUMO levels closer to the Fermi level of silver nanoparticles were readily detected, whereas those with more distant LUMO levels produced negligible SERS signals under identical conditions. This study provided direct evidence that the LUMO–Fermi gap governs hot-electron transfer efficiency and thereby determines whether charge-transfer-assisted SERS can occur.

Building on this framework, the present study investigates ketoprofen and trimethoprim as model pharmaceutical pollutants. These analytes are environmentally relevant, mechanistically complementary, and analytically instructive. Interestingly, their calculated LUMO levels are relatively similar, which provides an opportunity to test how SERS detectability depends not only on orbital alignment but also on adsorption characteristics. In particular, when the energy-level landscape is not strongly differentiating, differences in anchoring groups and molecular orientation may determine the reproducibility and intensity of the SERS response.

Here we compare the SERS responses of ketoprofen and trimethoprim on silver nanostructures, aiming to rationalize their performance through adsorption behavior and energy-level considerations. Beyond mechanistic understanding, we seek to identify strategies for improving the weaker SERS response, thereby expanding the range of pharmaceutical analytes amenable to reliable SERS detection. Finally, we extend our evaluation beyond model aqueous solutions to include commercial medicinal products, demonstrating the applicability of SERS not only for environmental monitoring but also for pharmaceutical quality control and counterfeit detection.

2. Materials and methods

2.1. Chemicals

Sodium chloride (NaCl, 99%) and sodium citrate ($Na_3C_6H_5O_7$, 99.9%) were purchased from Xilong Scientific Co. Ltd, China. Ketoprofen (>98%) and trimethoprim (>98%) were provided by Sigma-Aldrich. All chemicals were used as received without further purification. Two silver plates were prepared with dimensions of (100 mm × 5 mm × 0.5 mm). All experiments were performed with double-distilled water.

2.2. Synthesis of colloidal silver nanoparticles and their characterizations

e-AgNPs were synthesized using a modified electrochemical method as previously reported.[21] The electrochemical process was carried out in a beaker containing 200 mL of 0.1% $Na_3C_6H_5O_7$ solution in distilled water, serving as both the electrolyte and surfactant. Prior to use, silver electrodes were mechanically polished and rinsed with distilled water to remove surface oxides. Two prepared silver plates were then positioned vertically, face-to-face, and connected as electrodes. Electrolysis was performed under a constant DC voltage of 12 V at 200 °C with uniform magnetic stirring at 200 rpm for 2 h. The resulting colloidal e-AgNP solution displayed the characteristic grayish-yellow color. The morphology of the e-AgNPs was characterized by scanning electron microscopy (SEM, Hitachi S-4800) operated at 5 kV, revealing spherical nanoparticles with an average diameter of 24 nm. UV–Vis absorption spectra were collected using a JENWAY 6850 spectrophotometer with 10 mm path length quartz cuvettes.

2.3. Cyclic voltammetry measurement

Cyclic voltammetry (CV) experiments were conducted on a Palmsens 4 electrochemical workstation under ambient conditions. The setup followed a previously reported procedure, employing a platinum working electrode and an Ag/AgCl reference electrode.[22] A 0.1 M phosphate buffer solution (PBS) was used as the supporting electrolyte. All potentials were calibrated against the Fc/Fc$^+$ internal standard. CV measurements of the analytes were recorded within the potential window of −2.0 to 2.0 V at a scan rate of 50 mV s^{-1}.

2.4. Refractive-index sensitivity (RIS) and electromagnetic stability analysis

To assess the electromagnetic (EM) stability of the e-AgNP substrate, the refractive-index sensitivity (RIS) was determined by recording extinction spectra of e-AgNP colloids in glycerol-water mixtures with different volume fractions (0–32% v/v) at 25 °C. The refractive index (n) of each mixture was measured using a handheld refractometer (±0.001 RIU). The localized surface plasmon resonance (LSPR) peak position (λ_{max}) was extracted from the extinction spectra by Lorentzian fitting, and the slope of λ_max versus n was taken as the RIS (in nm RIU^{-1}). To evaluate the effect of analyte adsorption, extinction spectra of e-AgNPs containing trimethoprim (TMP) and ketoprofen (KTP) (1.75×10^{-4} M) were measured under identical conditions, and the corresponding LSPR shifts were used to estimate the effective local refractive-index changes at the nanoparticle surface. Based on these data, the variation of the EM field at the excitation wavelength (785 nm) was estimated to be less than 1%, confirming that EM conditions remained stable during SERS measurements.

2.5. Substrate preparation and SERS measurements

Aluminum (Al) substrates ($1 \times 1 \times 0.1$ cm) featuring a circular surface-active area (0.2 cm diameter) were fabricated. The substrates were rinsed with ethanol and dried at room temperature (RT). SERS-active solutions were drop-casted onto the surface-active area and dried at RT. KTP and TMP solutions were prepared in distilled water.

For each SERS measurement, 5 μL of analyte solution was deposited onto the prepared substrate and dried naturally at RT. Raman spectra were collected using a MacroRaman™ spectrometer (Horiba) with 785 nm laser excitation. Measurements were carried out with a $100\times$ objective (NA = 0.90), giving a diffraction-limited laser spot diameter of 1.1 μm (1.22λ/NA) and a focal depth of 115 nm. The laser power at the sample was 45 mW at a 45° incidence angle. Each spectrum was acquired with a 10 s exposure time and three accumulations, and the final spectra were obtained after baseline correction.

For chloride-assisted SERS measurements, 5 μL of NaCl solution was added onto the substrate 2 min after analyte deposition.

For real-sample analysis, tablets containing TMP and KTP were purchased from local pharmacies, ground, and mixed with water to obtain solutions with concentrations of 10^{-5} M, assuming the labeled contents were accurate. 5 μL of each solution was drop-casted onto the prepared substrate for SERS measurements.

2.6. Adsorption of TMP and KTP onto e-AgNPs

The adsorption of on the SERS substrates was monitored by UV–Vis spectroscopy. A 500 μL aliquot of TMP or KTP solution (1.05×10^{-3} M) was added to 2.5 mL of e-AgNP (100 ppm), allowing the solution of TMP or KTP to be diluted to be 1.75×10^{-4} M. Absorption spectra were recorded immediately after mixing and subsequently at 5–10 min intervals, continuing until the intensity of the characteristic absorption bands reached a steady state. To determine the concentration of analyte which did not adsorb onto e-AgNPs, the e-AgNP–analyte mixtures were centrifuged at 12 000 rpm for 10 min to remove nanoparticles and minimize scattering. The supernatant was used to determine residual analyte concentration by the Beer–Lambert law.

3. Results and discussion

3.1. Characterization of e-AgNPs

The formation and structural characterization of e-AgNPs were monitored using UV-visible absorption spectroscopy. Fig. 1a displays an absorption spectrum of AgNPs that the spectrum exhibits a sharp and symmetric surface plasmon resonance (SPR) band centered at 402 nm give a sharp peak at 409 nm after 3 h of electrochemical synthesis. This band originates from the collective oscillation of conduction electrons at the nanoparticle surface[23] and is highly sensitive to particle size, shape, and degree of aggregation. The presence of a single, narrow peak suggests that the product consists of well-dispersed spherical nanoparticles with minimal agglomeration.[24] The symmetry of the plasmon band further implies that the colloid is stable, which is a prerequisite for generating reproducible SERS signals.[25] The crystalline structure along with the lattice characteristics of the e-AgNPs was investigated using the X-ray diffraction method. The X-ray diffraction pattern of e-AgNPs displays three sharp diffraction peaks at $2\theta = 38.13°$, 44.32°, and 64.55° (Fig. 1b). These 2θ values in the spectrum, corresponding to the (111), (200), and (311) diffraction planes, respectively, relate to the patterns of the face-centered cubic (FCC) and crystalline structure of e-AgNPs. The dominant diffraction peak was observed at the (111) plane, indicating the preferred crystallographic orientation of the nanoparticle structure.[26] Moreover, the morphology of the nanoparticles was further visualized by scanning electron microscopy (SEM). As shown in Fig. 1c, the particles are nearly spherical with uniform size distribution and an average diameter of approximately 50 nm. Several research groups obtained the highest SERS enhancement for probe molecules such as Rhodamine 6G and Rhodamine B when using the e-AgNPs with an optimal particle size of approximately 50 nm.[27,28] The combined structural, optical, and morphological characterization confirms that the synthesized e-AgNPs possess the critical features required for efficient SERS substrates: (i) a well-defined and stable plasmon resonance, (ii) high crystallinity with preferential (111) facet exposure, and (iii) uniform particle size around 50 nm, consistent with literature reports of maximum SERS enhancement.

e-AgNPs were employed as the active SERS substrate for detection of trimethoprim (TMP) and ketoprofen (KTP) in the
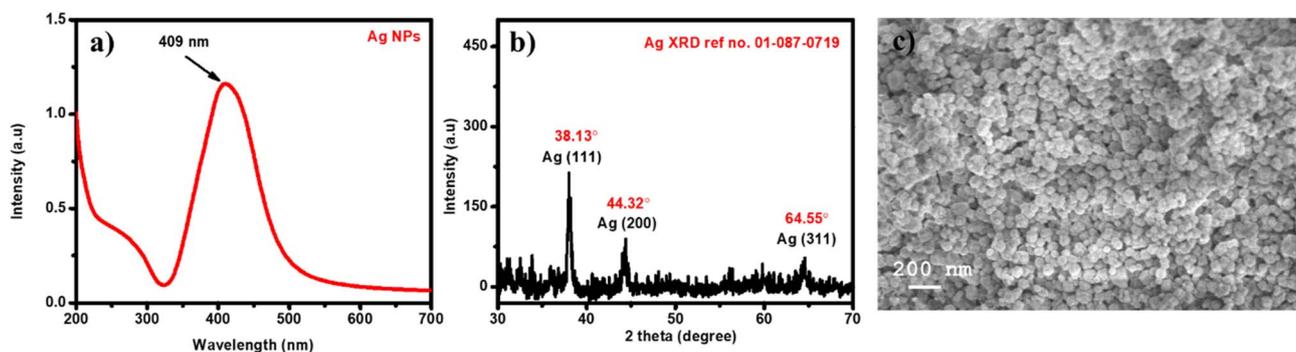

Fig. 1 Characterization of e-AgNPs (a) absorption spectrum, (b) XRD pattern and (c) SEM image of Ag nanoparticles.

following sections. We used the same e-AgNP substrate for all measurements to minimize EM variability arising from particle size, shape, distribution, and illumination. Because adsorption can still induce a small LSPR perturbation, the residual EM variation was quantified in Section 3.2. Unless noted otherwise, analyte-to-analyte differences are discussed in terms of electronic (charge-transfer) and adsorption effects.

3.2. Electromagnetic stability and electrochemical estimation of frontier orbital energies of trimethoprim and ketoprofen

As described in Section 2.4, the e-AgNPs were immobilized on aluminum substrates by drop-casting and drying, after which the analyte solution was applied. In the EM mechanism of SERS, the measured intensity scales approximately with the fourth power of the local electric field amplitude, so small changes in plasmon detuning can rescale intensity by only a few percent.[29] To verify EM stability on our e-AgNP substrate, we first determined the refractive-index sensitivity (RIS) by recording extinction spectra in glycerol–water standards (0–32% v/v, 25 °C),[30] measuring the bulk refractive index of each mixture (n) with a refractometer, and extracting the LSPR peak of e-AgNPs in the mixture (λ_{max}) via Lorentzian fits (Fig. S2a). A

linear regression of λ_{max} *versus* n is shown in Fig. S2b, in which RIS is the slope. RIS, therefore, was estimated to be 151.04 nm RIU^{-1}. Beside, absorption spectra of e-AgNPs in the presence of TMP and KTP (1.75×10^{-4} M) was also recorded and compared to that of pure e-AgNPs (Fig. S2c). The adsorption of those analytes onto the surface of e-AgNPs led to some differences in the LSPR bands. To be detailed, in the presence of TMP, a blue shift of 1 nm was observed ($\delta\lambda_0 = -1$ nm), meanwhile, a red shift of 0.5 nm was detected in the presence of KTP in the e-AgNP solutions ($\delta\lambda_0 = 0.5$ nm). These shifts were converted into the effective local refractive-index change at the e-AgNP surface (Δn) using the equation:

$$\Delta n = \frac{\delta\lambda_0}{RIS} \tag{1}$$

TMP gives a Δn of -0.0066 RIU, representing slightly decreased effective polarizability consistent with electron-donating coordination while KTP gives a Δn of 0.0033 RIU, associated with slight dielectric loading. However, these values are small ($|\Delta n| < 0.01$ RIU). At 785 nm excitation, far from the Ag LSPR, the detuning is $\Delta = \lambda_{ex} - \lambda_0 = 785 - 409 = 376$ nm. For small peak shifts, under large detuning, the off-resonant EM factor at the laser wavelength is bounded by
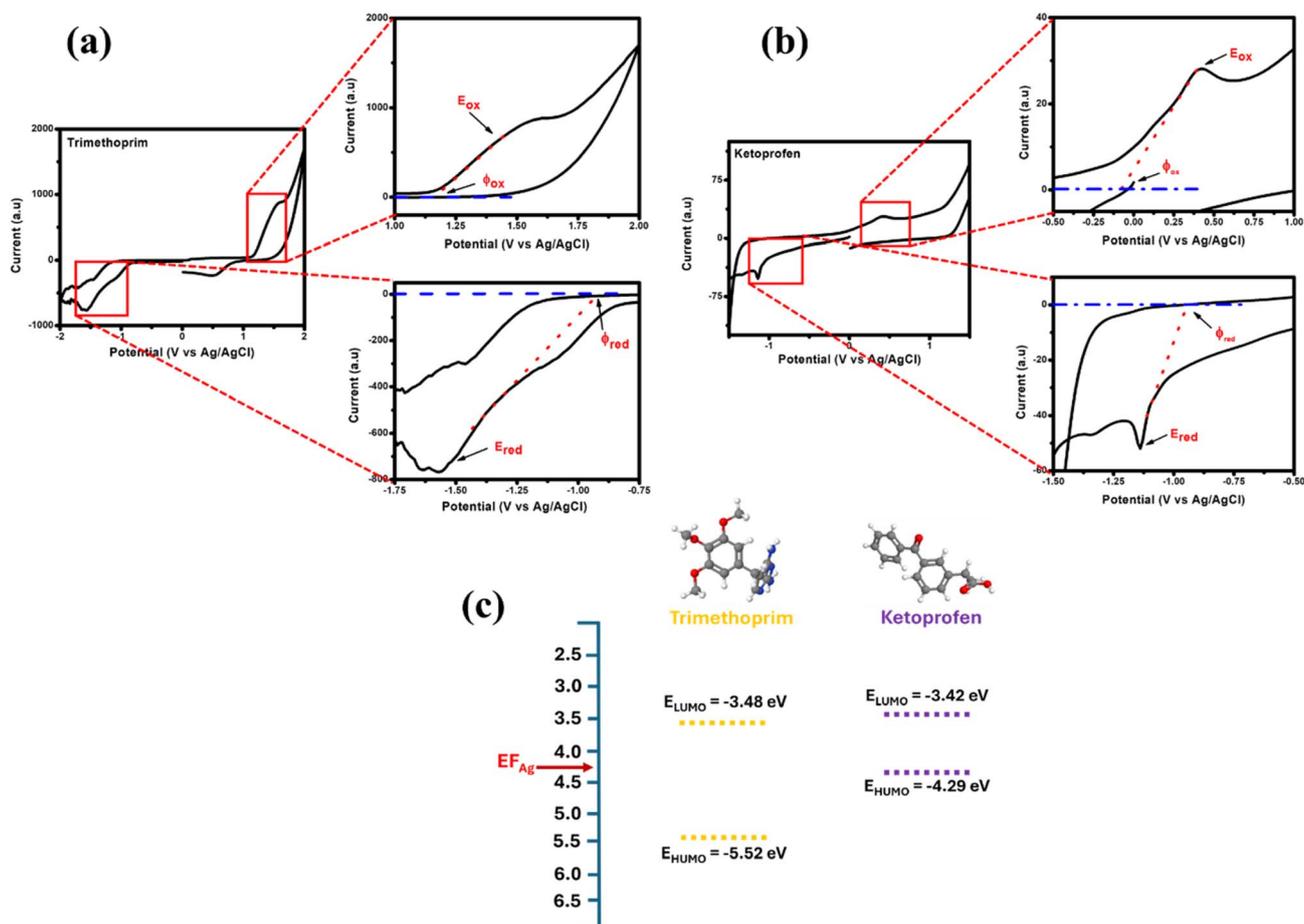

Fig. 2 Cyclic voltammograms of the (a) TMP, (b) KTP dissolved in PBS, and (c) the LUMO energy level of TMP, KTP on their SERS signals.

$$\frac{G_{EM,after}}{G_{EM,before}} \approx \left(\frac{\Delta}{\Delta - \delta\lambda_0}\right)^4 \tag{2}$$

The off-resonant EM factors for TMP and KTP was calculated to be 0.989 and 1.005 hence, EM variation is limited to about 1%. Thus, the e-AgNP substrate provides effectively stable EM conditions for both analytes.

Concerning CM contribution, in a previous study, we demonstrated that analytes with LUMO levels closely aligned with the silver Fermi level exhibited strong SERS responses, while those with more distant LUMO levels produced negligible enhancement under identical conditions.[20] This finding underscored the decisive role of the gap between LUMO levels of the analyte and the Fermi level of Ag in enabling CT-assisted SERS.

To evaluate this factor for TMP and KTP, cyclic voltammetry (CV) was employed to determine their onset oxidation and reduction potentials (ϕ_{ox} and ϕ_{red}). These values were converted to HOMO and LUMO energy levels using the following relations:[22,31,32]

$$E_{HOMO} = -e(\phi_{ox} + 4.8 - \phi_{Fc/Fc^+}) \tag{3}$$

$$E_{LUMO} = -e(\phi_{red} + 4.8 - \phi_{Fc/Fc^+}) \tag{4}$$

where which ϕ_{Fc/Fc^+} presents the redox potential of ferrocene/ferrocenium couple (Fc/Fc^+) in the electrochemical system, assuming the energy level of Fc/Fc^+ to be −4.8 eV below vacuum level, taken as 0.44 V *versus* Ag/AgCl in this system.[22]

For TMP, the CV curve (Fig. 2a) exhibited an onset oxidation potential of 1.17 V and an onset reduction potential of −0.92 V, yielding HOMO and LUMO levels of −5.52 eV and −3.48 eV. For KTP, oxidation and reduction onsets were observed at −0.07 V and −0.95 V (Fig. 2b), corresponding to HOMO and LUMO levels of −4.29 eV and −3.42 eV.

As illustrated in Fig. 2c, both analytes possess LUMO levels that are closely aligned with the Fermi level of silver (−4.26 eV), with energy gaps of 0.78 eV for TMP and 0.84 eV for KTP. The small difference of only 0.06 eV indicates that hot-electron transfer from the e-AgNP substrate to the analyte LUMO is energetically feasible for both molecules. Based on this electronic alignment, comparable SERS responses would be anticipated for TMP and KTP under identical experimental conditions.

3.3. Comparative SERS performance of TMP and KTP

The SERS spectra of TMP and KTP were recorded on e-AgNP substrates under identical experimental conditions to evaluate whether their nearly identical LUMO levels (Section 3.2) translate into comparable detectability. Representative spectra at concentrations from 10^{-3} to 10^{-5} M are shown in Fig. 3. TMP exhibited multiple strong and reproducible bands, including peaks at 482 cm^{-1}, 593 cm^{-1}, 785 cm^{-1} and 1325 cm^{-1}, which are associated with –NH$_2$ bending, in-plane pyrimidine stretching, pyrimidine ring breathing, and C–O/C–C benzenic stretching, respectively. Among these, the band at 785 cm^{-1} is the dominant feature, remaining clearly detectable even at 10^{-5} M. These observations are consistent with vibrational spectroscopic
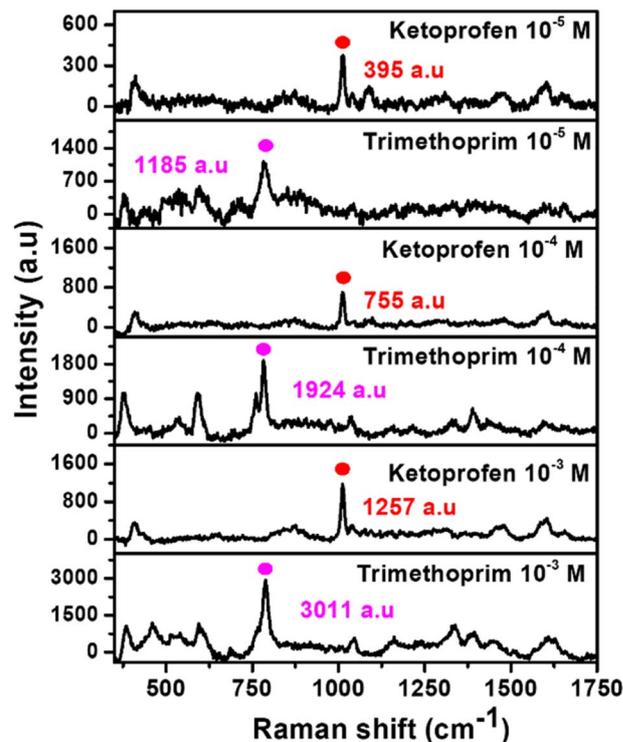

Fig. 3 Comparative SERS spectra of TMP and KTP on e-AgNP substrates at concentrations from 10^{-3} to 10^{-5} M.

and DFT analyses of TMP.[33] In contrast, KTP produced weaker and less reproducible SERS signals. Faint features were observed at 704 cm^{-1} (C–H deformation; CH$_3$ rocking), 1004 cm^{-1} (Φ–C–C–Φ symmetric stretch, phenyl breathing), 1031 and 1138 cm^{-1} (ring deformation), 1194 cm^{-1} (C–C stretching), and 1598 cm^{-1} (aromatic ring stretching). Among them, the 1004 cm^{-1} phenyl breathing band was the most prominent, but its intensity was considerably lower than the dominant TMP band under equivalent conditions. These assignments agree with earlier Raman and DFT analyses of KTP.[34,35]

The overall comparison demonstrates that TMP is readily detected on e-AgNP substrates, whereas KTP yields only weak responses, despite their nearly identical LUMO–Fermi gaps. This discrepancy indicates that adsorption geometry and anchoring chemistry are the decisive factors governing SERS activity when electronic alignment alone is not discriminating. Furthermore, our analysis of the electromagnetic (EM) contribution (Section 3.2) showed that EM variation is limited to about 1%, far below the 2–3-fold difference in SERS intensity between TMP and KTP. These results confirm that the observed contrast originates primarily from charge-transfer-mediated chemical enhancement and adsorption geometry, rather than from EM fluctuation.

3.4. Adsorption-driven differences in SERS response of TMP and KTP

The contrasting SERS performances of TMP and KTP, despite their nearly identical LUMO levels (Fig. 2c), indicate that

electronic alignment alone cannot account for their detectability. Instead, adsorption pathways and surface interactions with AgNPs could have play an important role.

Concerning TMP, multiple anchoring groups are available, most importantly the pyrimidine nitrogen atoms. Experimental SERS combined with under this fixed-substrate configuration, the EM enhancement under this fixed-substrate configuration, the EM enhancement DFT calculations have demonstrated that TMP preferentially adsorbs onto Ag surfaces *via* its pyrimidine ring nitrogens, adopting a near-perpendicular orientation (Fig. 4) that promotes strong chemisorption and efficient charge transfer.[33] The dominance of the 785 cm^{-1} pyrimidine breathing mode in the SERS spectra of TMP (Fig. 3) is consistent with this geometry, since SERS surface selection rules predict enhanced intensity for vibrations directly coupled to adsorption sites.[36] In addition to pyrimidine coordination, the amino substituents of TMP can weakly interact with Ag through lone-pair donation, further stabilizing the adsorption complex,[37,38] while the methoxy groups and aromatic rings play mainly electronic and conjugative roles.[37,39] Taken together, this binding model explains why TMP exhibits intense and reproducible SERS features, particularly the persistent 785 cm^{-1} band that remains detectable even at 10^{-5} M.

By contrast, KTP relies primarily on its carboxylate group for adsorption. While carboxylates can bind to Ag, the bulky aromatic framework of KTP restricts the molecule from adopting a flat orientation (Fig. 4), forcing a tilted geometry that limits electronic coupling with the Ag surface. The consequence is that only intrinsically strong Raman modes, such as the phenyl breathing vibration around 1004 cm^{-1}, remain observable, but with much lower intensity and reproducibility than TMP (Fig. 3). This interpretation is consistent with SERS studies of aromatic carboxylates, which demonstrate that steric hindrance or substituent position can enforce tilted adsorption modes and attenuate SERS signals,[40] in contrast to unhindered flat adsorption through the aromatic π-system.[36,41]

Taken together, these results indicate that while TMP benefits from multiple nitrogen donor groups enabling strong chemisorption and effective orbital overlap with Ag, KTP suffers from restricted adsorption geometry and limited anchoring. Thus, when LUMO–Fermi alignment does not discriminate between analytes, adsorption geometry and anchoring functionality dictate SERS detectability.

To further support this statement, we compared the adsorption behavior of TMP and KTP on e-AgNPs using UV–vis

absorption spectroscopy. The adsorption process was monitored following the absorption model described in Section 2.5. The time-dependent changes in the absorption intensity of TMP and KTP solutions (1.75 × 10^{-4} M) in the presence of e-AgNPs are shown in Fig. 5a and b, respectively. For TMP, the characteristic absorption band at 270 nm decreased progressively with increasing incubation time, indicating adsorption of TMP molecules onto the surface of e-AgNPs. In contrast, the absorption intensity of KTP at 260 nm decreased only by 3% before reaching a steady state after 30 min of incubation (Fig. 5e), confirming its weaker adsorption affinity. As mentioned in Section 2.5, parallel experiments were performed to these sample sets as the colloidal-analyte mixtures were centrifuged at 12 000 rpm for 10 min to remove nanoparticles and minimize scattering. The absorption spectra of the supernatants showed a slight decrease in intensity but no spectral shift after centrifugation (Fig. 5c and d). A similar trend of decreasing in adsorption intensity at 260 nm for KTP and 270 nm of TMP was also recorded as shown in Fig. 5e.

On the other hand, along with these changes in the molecular absorption bands, we also observed distinct differences in the SPR band of e-AgNPs during incubation with the two analytes. In the presence of TMP, the LSPR intensity of e-AgNPs decreased significantly, consistent with surface coverage by TMP molecules. Moreover, a slight blue shift of the SPR band was detected within the first 50 minutes of incubation, and the absorption spectra of the TMP–e-AgNP mixture during this period exhibited a clear isosbestic point at 504 nm (Fig. 5a), indicative of a well-defined adsorption equilibrium process, in which TMP has replaced citrate on the surface of e-AgNPs. After 50 minutes of incubation, the intensity of SPR band continued to drop and the band was broadening due to the interaction of TMP and e-AgNPs. In contrast, such spectral features were absent in the KTP–e-AgNP mixture, further highlighting the limited interaction between KTP and e-AgNPs.

The adsorption capacity of the adsorbate, q_e, defined as the amount of analyte adsorbed per unit mass of adsorbent at equilibrium (mg g^{-1}), was calculated according to the well-known relation:

$$q_e = \frac{(C_i - C_e) \times V}{m} \tag{5}$$

where C_i (mg L^{-1}) and C_e (mg L^{-1}) are the initial and equilibrium concentrations of the adsorbate in solution, respectively, V (L) is the volume of the solution, and m (g) is the mass of the adsorbent used.

This equation could be employed to estimate the adsorption capacities of TMP and KTP onto e-AgNPs in solution. $C_{i\text{-TMP}}$ and $C_{i\text{-KTP}}$ are the initial concentrations of TMP and KTM in the mixtures, respectively, as mentioned in Section 2.3, $C_{i\text{-TMP}} = 1.75 \times 10^{-4}$ $M \approx 50.8$ mg L^{-1} and $C_{i\text{-KTP}} = 1.75 \times 10^{-4}$ $M \approx 44.5$ mg L^{-1}. $C_{e\text{-TMP}}$ and $C_{i\text{-KTP}}$ were calculated based on the absorption at 270 nm and 260 nm, respectively, of the mixture at the equilibrium state using the Beer–Lambert law:
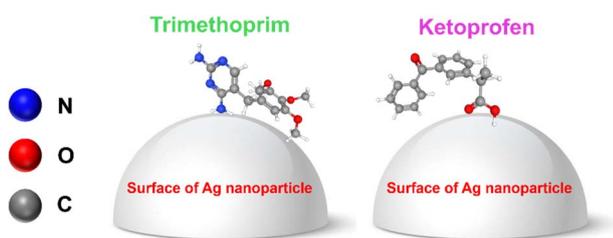
$$A = \varepsilon l c \tag{6}$$

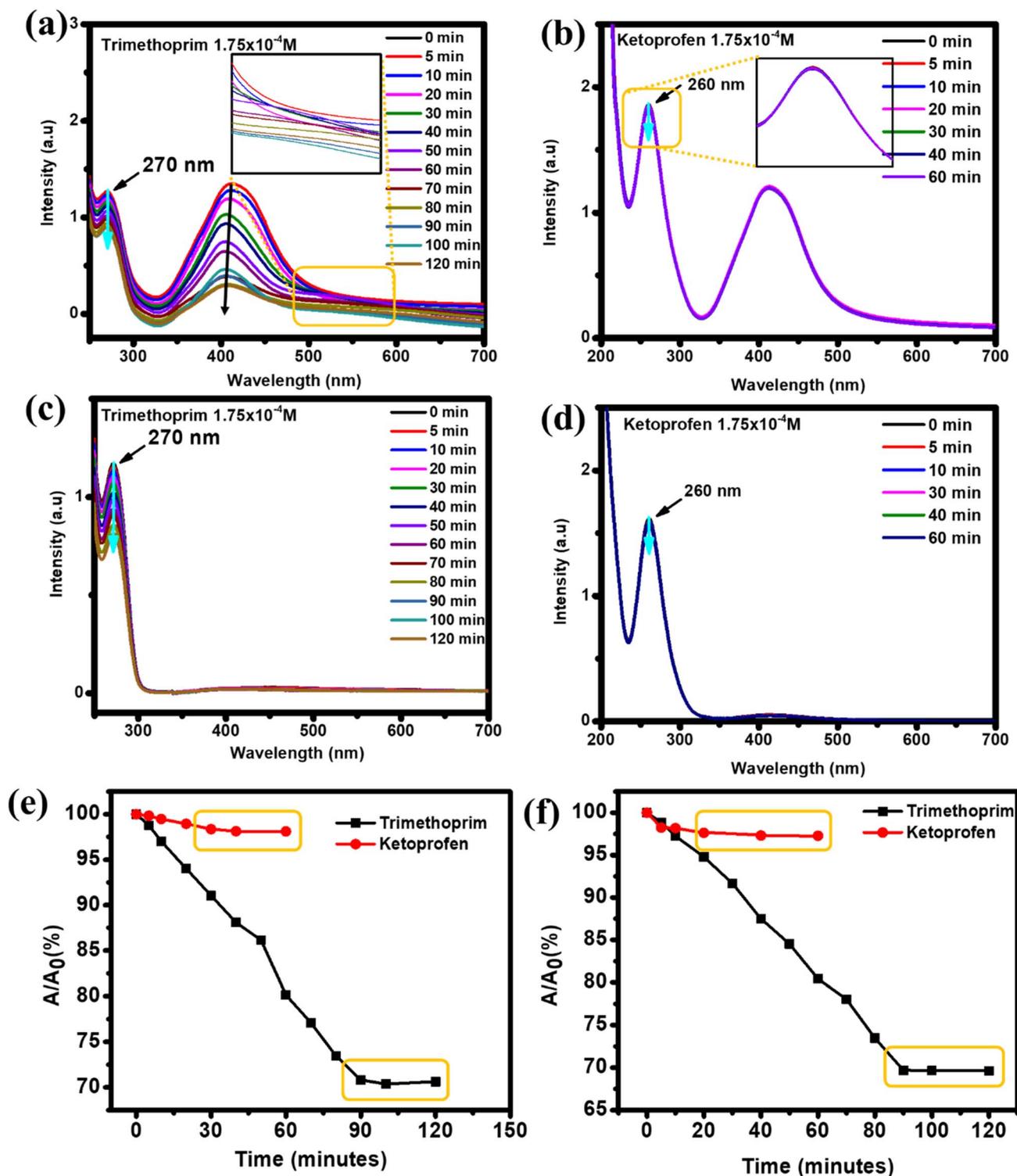**Fig. 4** Surface interaction between Ag and trimethoprim (TMP), ketoprofen (KTP) molecules.

Fig. 5 Absorption spectra of the (a) TMP, and (b) KTP (1.75×10^{-4} M) in e-AgNP solutions over an incubation period of 120 min, 60 min, respectively; Absorption spectra of the (c) TMP, and (d) KTP (1.75×10^{-4} M) after the removal of e-AgNPs over an incubation period of 120 min, 60 min in e-AgNP solutions, respectively; changes in absorption intensity at 270 nm for the TMP and 260 nm for the KTP with the time of incubation (e) with and (f) without centrifugation to remove e-AgNPs.

in which A is absorbance; ε (L mol^{-1} cm^{-1}) is the molar absorption coefficient; l (cm) is the optical path length; and c (mol L^{-1}) is concentration of the solution. The average molar absorption coefficients of TMP and KTP solutions were calculated using their absorption intensities at 270 and 260 nm, respectively (Fig. S1), and determined to be 7.5×10^4 and $11.6 \times$

10^4 L mol^{-1} cm^{-1}. Hence, the equilibrium concentrations $C_{e\text{-}TMP}$ and $C_{e\text{-}KTP}$ were calculated to be 31.3 mg L^{-1} and 34.8 mg L^{-1}, respectively. Therefore, the adsorption capacities of TMP and KTP on e-AgNPs in solution were calculated to be 390.1 mg g$^{-1} \approx 1.3 \times 10^{-3}$ mol g^{-1} and 198.3 mg g$^{-1} \approx 7.8 \times 10^{-4}$ mol g^{-1}, respectively, indicating that at the equilibrium state, the maximum number of TMP molecules adsorbed on e-AgNPs is nearly 4-time higher than that of KTP molecules. Although the experiment was performed in an aqueous environment, which differs from the real SERS condition where e-AgNPs are dried and immobilized prior to analyte addition, the UV-vis measurements still provide valuable insight into the relative adsorption affinities of TMP and KTP. The time-dependent decrease in absorbance reflects the intrinsic tendency of each analyte to interact with AgNP surfaces. Thus, even though the absolute adsorption kinetics may differ between colloidal and immobilized systems, the comparative results confirm that TMP exhibits a much stronger and more sustained interaction with AgNPs than KTP, in agreement with the SERS observations.

Despite the poor performance of e-AgNP-based SERS sensors for KTP under baseline conditions, the persistence of KTP residues in the environment represents a significant ecological risk that necessitates detection at trace levels. Since the intrinsic
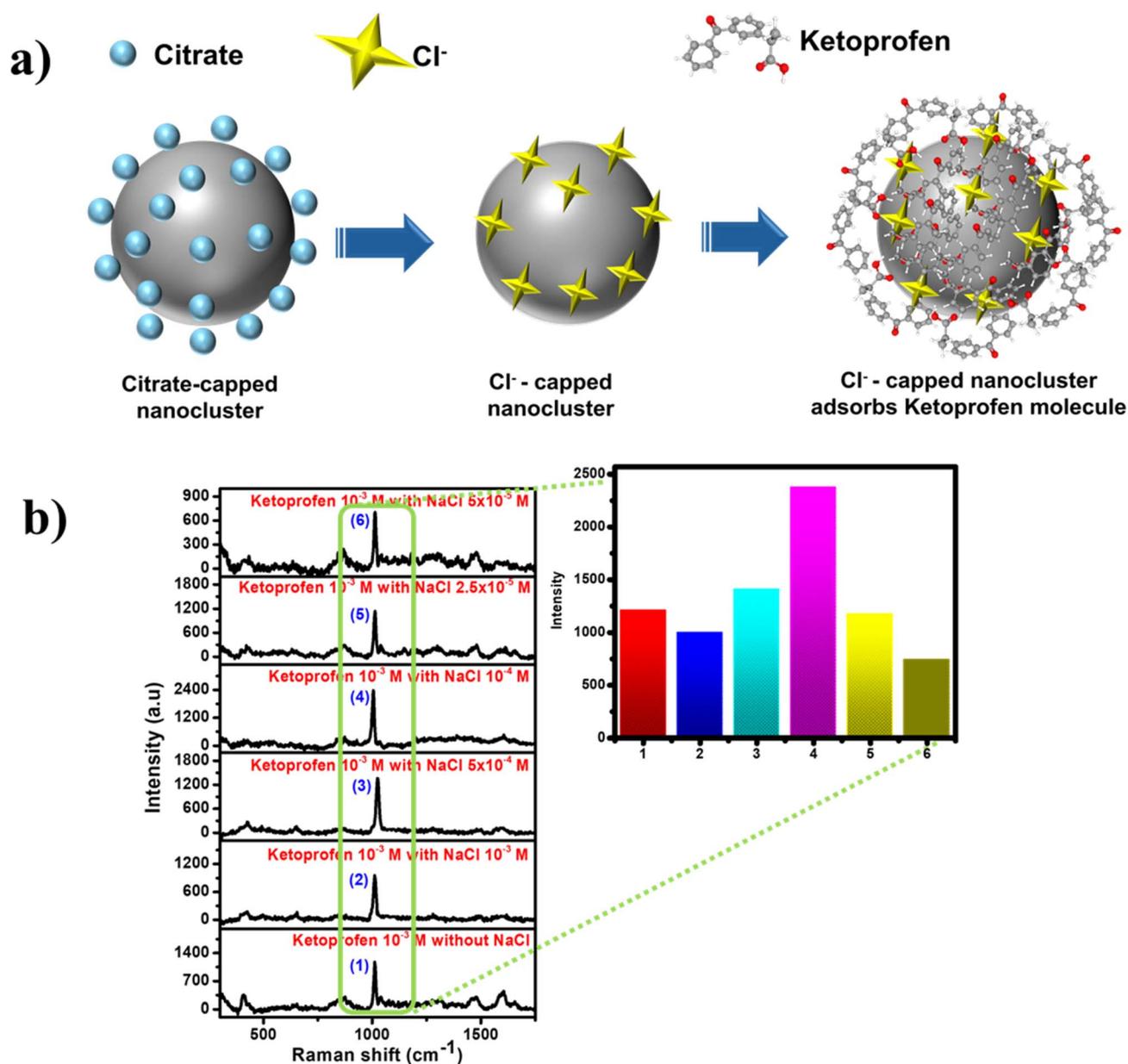

Fig. 6 (a) Schematic illustration of chloride activation: from citrate–capped to Cl$^-$-capped Ag nanoclusters, enabling ketoprofen adsorption and SERS activation. (b) SERS spectra of ketoprofen (10^{-3} M) recorded on immobilized e-AgNP substrates in the absence of chloride and after the addition of NaCl at 10^{-3} M, 5×10^{-4} M, 10^{-4} M, 5×10^{-5} M and 10^{-5} M. The inset shows the intensity of the 1004 cm^{-1} phenyl breathing band as a function of chloride concentration.

molecular properties of KTP cannot be altered, an effective strategy is to modify the interfacial chemistry of e-AgNPs to promote stronger adsorption. In the following section, we demonstrate that the addition of chloride ions serves this role by activating the Ag surface, thereby enhancing adsorption and enabling reliable SERS detection of KTP.

3.5. Chloride-assisted improvement of KTP detectability on e-AgNP substrates

As established in Section 3.3, KTP exhibits weak SERS activity on e-AgNP substrates due to limited adsorption affinity, despite possessing a LUMO level comparable to TMP. To overcome this limitation, we investigated whether chloride ions could activate the Ag surface and improve KTP detection. The experiment was performed by first allowing KTP molecules (10^{-3} M) to adsorb onto immobilized e-AgNPs for 2 min, followed by the addition

of NaCl at varying concentrations. Fig. 6b presents the SERS spectra of KTP recorded in the absence and presence of NaCl (5×10^{-5}–10^{-3} M). In the absence of chloride, only a weak signal was observed, with the 1004 cm^{-1} phenyl ring breathing band showing an intensity of around 1200 a.u. The addition of NaCl led to a marked enhancement of the SERS response. The intensity increased progressively, reaching a maximum at 10^{-4} M NaCl, where the intensity of the band at 1004 cm^{-1} rose to nearly 2500 a.u., which is nearly 2.5-fold higher than that on the chloride-free system. At higher NaCl concentrations (5×10^{-4} M and 10^{-3} M), however, the SERS intensity decreased again. This decline cannot be attributed to colloidal aggregation, since the AgNPs were immobilized on the substrate prior to analyte addition. Instead, it reflects the delicate balance of chloride effects at the Ag interface. At low to moderate concentrations, chloride ions displace citrate ligands, compress
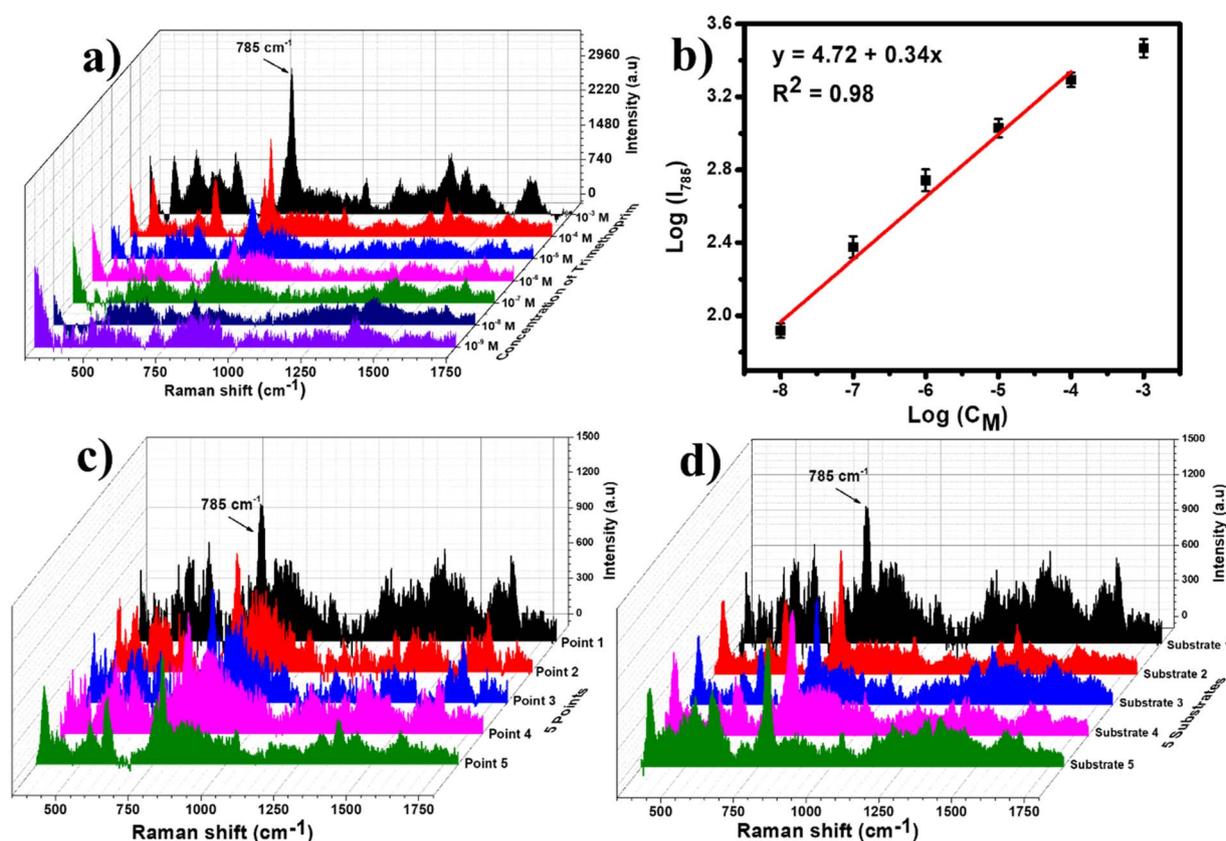

Fig. 7 (a) SERS spectra of TMP (10^{-3}–10^{-9} M) on AgNPs. (b) Plot of the log of SERS intensity at 785 cm^{-1} against TMP concentration. (c) Uniformity and (d) reproducibility of SERS sensors for TMP (10^{-5} M) using the AgNPs substrate.

Table 1 Several reported sensors for TMP

Sensor/type	Linear range	LOD	Ref.
MIP@Fe$_3$O$_4$@MWNTs/rGO/MCPE electrochemical sensors	4×10^{-9}–5×10^{-4} M	1.2×10^{-9} M	45
AuNPs–Printex(6L)–CTS:EPH/GCE voltammetric sensor	2×10^{-7}–6×10^{-6} M	1.24×10^{-8} M	46
ZnO/CPE electroanalytic sensor	—	2.58×10^{-8} M	47
TLC-SERS (AuNPs on TLC), chemometrics (MCR-ALS/ICA)	10^{-7}–5×10^{-6} M	10^{-7} M	48
e-AgNPs immobilized on	10^{-4}–10^{-8} M	3.84×10^{-9} M	This work

the electrical double layer, and form $AgCl_x^-$ surface states, thereby exposing fresh binding sites and facilitating charge transfer into the LUMO of KTP (Fig. 6a).[42] Such activation effects of halides on Ag colloids have been clearly demonstrated in early studies of chloride-treated silver sols[43] and later formalized in the adatom model, in which chemisorbed halides create intermediate surface states that enhance SERS.[42] When chloride is present in excess, however, surface over-coverage by Cl^- blocks available adsorption sites,[44] while strong electrostatic screening reduces the ability of KTP molecules to approach the surface. Thus, optimal enhancement occurs only within a narrow chloride concentration window, with 10^{-4} M providing the best balance between activation and stability. These results demonstrate that chloride ions can effectively "rescue" the SERS detectability of KTP by activating the Ag surface through interfacial chemical effects rather than structural changes to the immobilized e-AgNPs.

3.6. e-AgNP-based SERS sensors for analysis of TMP and KTP

The quantitative performance of the e-AgNP SERS substrates was evaluated for both TMP and KTP by constructing calibration curves based on the intensity of their dominant Raman bands. For TMP, the pyrimidine breathing mode at 785 cm^{-1} was used as the marker band. Fig. 7a shows the SERS spectra of TMP from 10^{-3} M to 10^{-9} M, demonstrating clear and concentration-dependent signals across six orders of magnitude. The logarithm of the SERS intensity plotted against the logarithm of the concentration yielded a linear relationship with the regression of $R^2 = 0.98$ (Fig. 7b). The limit of detection (LOD) was calculated to be 3.84×10^{-9} M. This LOD was confirmed by Fig. S3a, showing the SERS spectrum of TMP at 4×10^{-9} M on e-AgNPs, with detectable characteristic bands despite high signal-to-noise. For each calibration point, SERS spectra were recorded in quintuplicate to estimate experimental error. The uniformity of the e-AgNP substrates was verified by
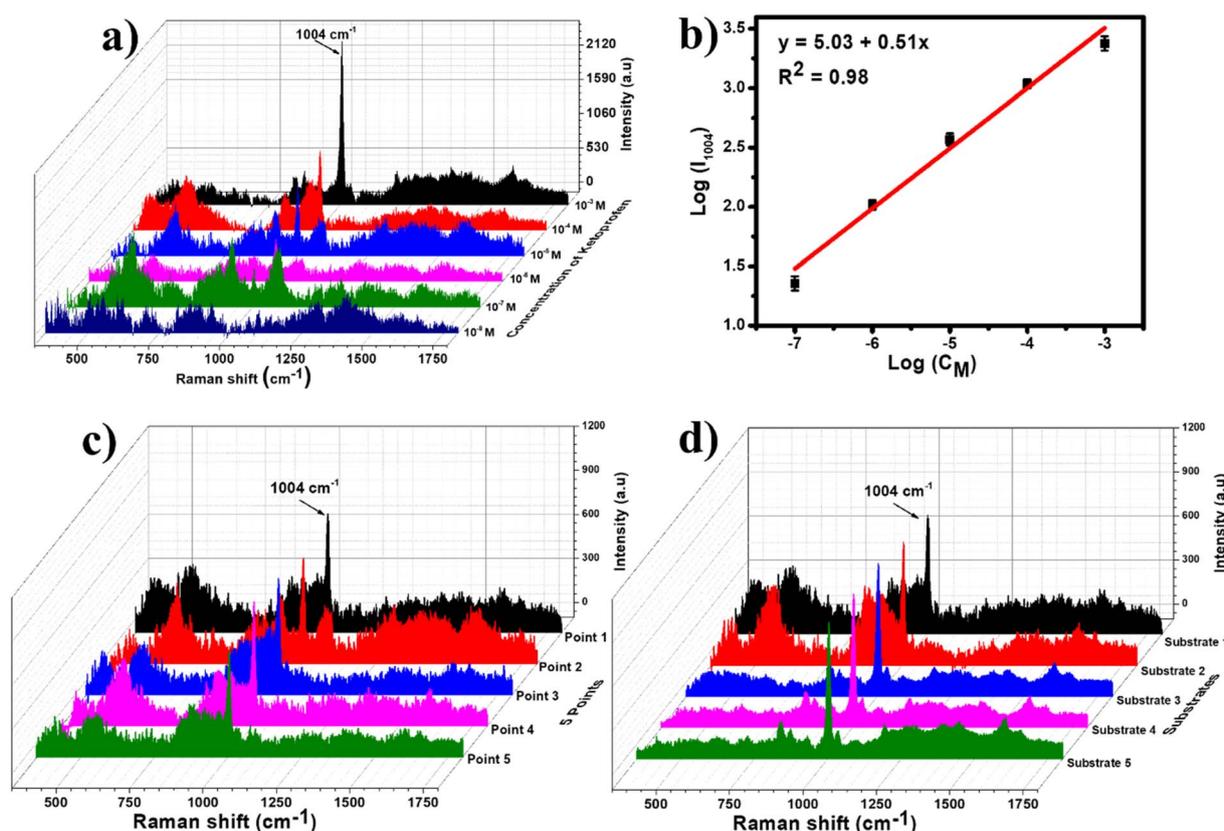

Fig. 8 (a) SERS spectra of KTP ($10^{-3}–10^{-8}$ M) on AgNPs. (b) Plot of the log of SERS intensity at 1004 cm^{-1} against KTP concentration. (c) Uniformity and (d) reproducibility of SERS sensors for KTP (10^{-5} M) using the AgNPs substrate.

Table 2 Several reported Ag-based SERS sensors to detect KTP

Materials/SERS substrates	LOD	Linear range	Ref.
Core–shell Ag nanotube arrays (Ag MeNTA)	10^{-6} M	$10^{-2}–10^{-6}$ M	49
L-cysteine capped AgNPs	4.5×10^{-6} M	$8 \times 10^{-6}–3 \times 10^{-5}$ M)	50
Ag/AZO film + AgNPs	0.01 ppm ($\approx 2.4 \times 10^{-5}$ M)	5–104 ppm ($\approx 2.4 \times 10^{-5}–5 \times 10^{-2}$ M)	51
e-AgNPs + NaCl activation	2.69×10^{-8} M	$10^{-7}–10^{-3}$ M	This work

recording spectra from five randomly chosen points on one substrate (Fig. 7c), resulting in a relative standard deviation (RSD) of 12.8%. Substrate-to-substrate reproducibility was further examined by testing five independently prepared AgNP substrates (Fig. 7d), yielding an RSD of 14.0%. These results demonstrate that TMP can be reliably quantified down to the nanomolar level using e-AgNP-based SERS. Although it does not achieve most impressive LOD, compared to electrochemical sensors, its LOD is lower than many reported sensors (Table 1). Moreover, the large linear range allows it to detect TMP at various concentrations. LOD and RSD values were calculated as presented in SI.

The same approach was applied to ketoprofen under optimized chloride activation conditions as a 10 μM of 10^{-4} M NaCl solution was drop-casted onto the SERS substrate for each measurement. Six KTP solutions ranging from 10^{-3} to 10^{-8} M were prepared and their SERS signals were recorded. Fig. 8a presents the SERS spectra, where the characteristic phenyl ring breathing band at 1004 cm^{-1} gradually decreased with concentration. The band was clearly detectable at 10^{-7} M but disappeared at 10^{-8} M. As shown in Fig. 8b, the logarithm of the SERS intensity plotted against the logarithm of the concentration yielded a linear relationship with the regression of $R^2 = 0.98$. Each measurement was performed in quintuplicate. The
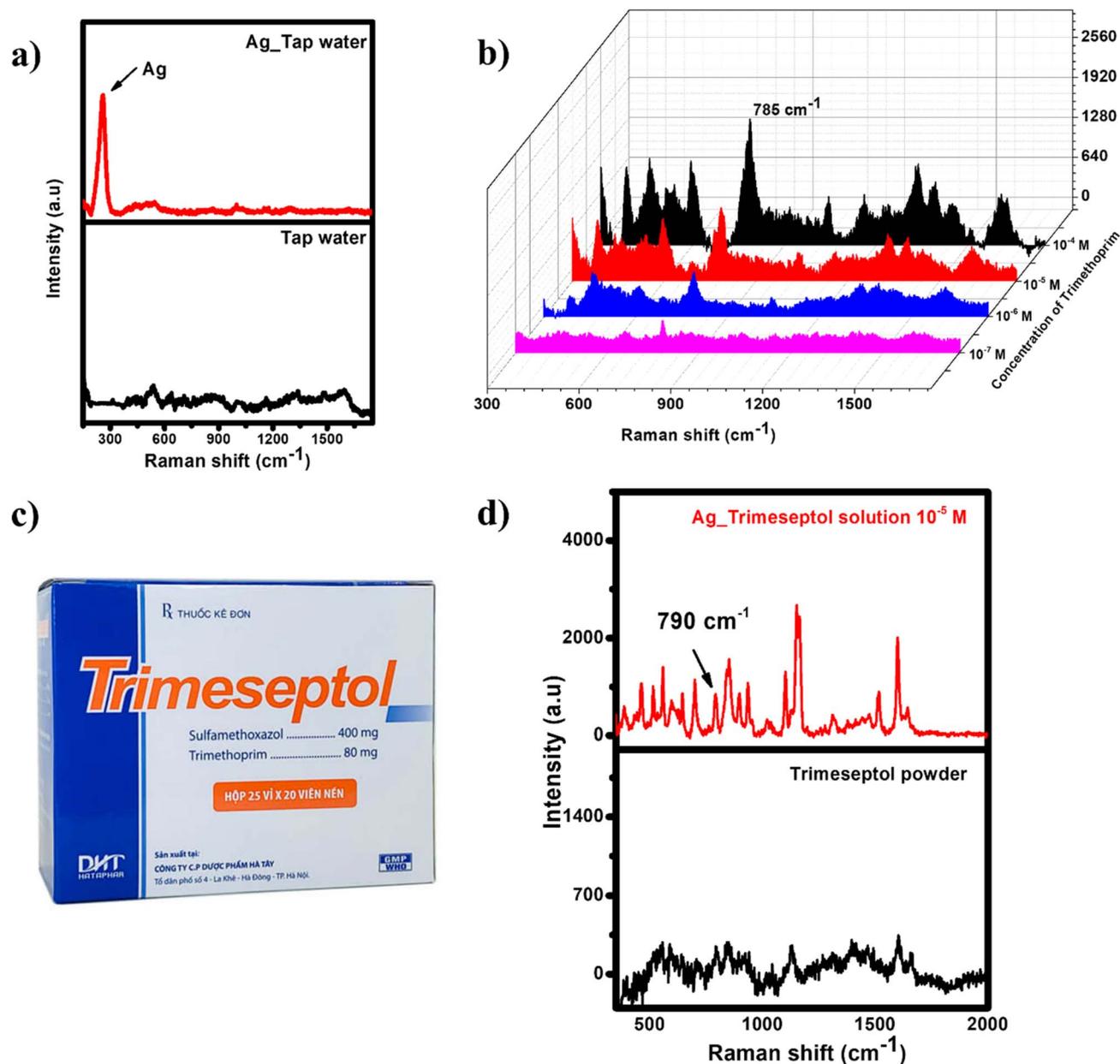

Fig. 9 (a) Raman spectra of tap water on e-AgNPs with (red) and without (black) e-AgNPs as SERS active substrates; (b) SERS spectra of TMP with different concentrations in tap water on e-AgNP SERS substrate; (c) commercial pharmaceutical production trimeseptol; (d) Raman spectra of trimeseptol solution, in which the concentration of TMP is approximately 10^{-5} M calculated based on establish TMP content, on e-AgNPs with (red) and without (black) e-AgNPs as SERS active substrates.

LOD was estimated as 2.69×10^{-8} M. Figure S3b shows SERS spectrum of TMP at concentration of 5×10^{-8} M, which is close to this LOD. In spite of high signal-to-noise, the characteristic bands of KTP are still detectable. The Substrate uniformity was assessed at 10^{-5} M by measuring five random points (Fig. 8c), giving an RSD of 12.5%. Reproducibility was evaluated across five independent e-AgNP substrates (Fig. 8d), with an RSD of 14.6%. These results confirm that although KTP adsorption is intrinsically weak, chloride activation allows sensitive and reproducible quantification down to tens of nanomolar concentrations, which is competitive to the reported SERS sensors as shown in Table 2. Besides, Fig. S4a and b compares the SERS performance of freshly prepared and 4 week stored substrates to detect TMP (10^{-5} M) and KTP (10^{-5} M), respectively. After 4 weeks of storage, the SERS intensities of the analytes only slightly decreased, revealing the recovery values of 92% for TMP and 94% for KTP sensors.

Taken together, these calibration experiments highlight the contrasting SERS detectability of the two pharmaceuticals. TMP achieves direct nanomolar detection on e-AgNP substrates due to strong adsorption through pyrimidine nitrogens, while KTP requires chloride-mediated surface activation to reach comparable levels of sensitivity and reproducibility.

3.7. Practicability of e-AgNP-based SERS sensors for TMP and KTP

To further evaluate the efficiency of the e-AgNP–based SERS sensors in real matrices, TMP was spiked into tap water at different concentrations ranging from 10^{-4} to 10^{-7} M. Fig. 9a presents the Raman spectra of tap water alone (black) and tap water on the e-AgNP substrate (red). As shown in Fig. 9b, the SERS spectra of TMP in tap water displayed the characteristic bands of TMP at 785 cm^{-1}. Quantitative recovery analysis yielded values between 89% and 96% (Table S1), confirming the reliability and accuracy of the e-AgNP–based SERS sensors for detecting TMP residues in real matrix of tap water.

To examine the detectability of the sensor in a more complex pharmaceutical sample, we measured TMP content in a commercial tablet, trimeseptol (Fig. 9c). Each tablet is labeled to contain two antibiotics: sulfamethoxazole (400 mg) and TMP (80 mg). The SERS spectrum of trimeseptol on e-AgNPs (Fig. 9d) showed multiple characteristic bands of sulfamethoxazole, including 830 cm^{-1} (aromatic C–H bending), 950 cm^{-1} (C–N–C vibrations), 1175 cm^{-1} (symmetric stretching of SO_2 group), 1580 cm^{-1} (C=C ring stretching) and 1620 cm^{-1} (C=C and C=N stretching).[52] The pyrimidine ring breathing band of TMP was also detected, slightly shifted to 790 cm^{-1}. Based on this
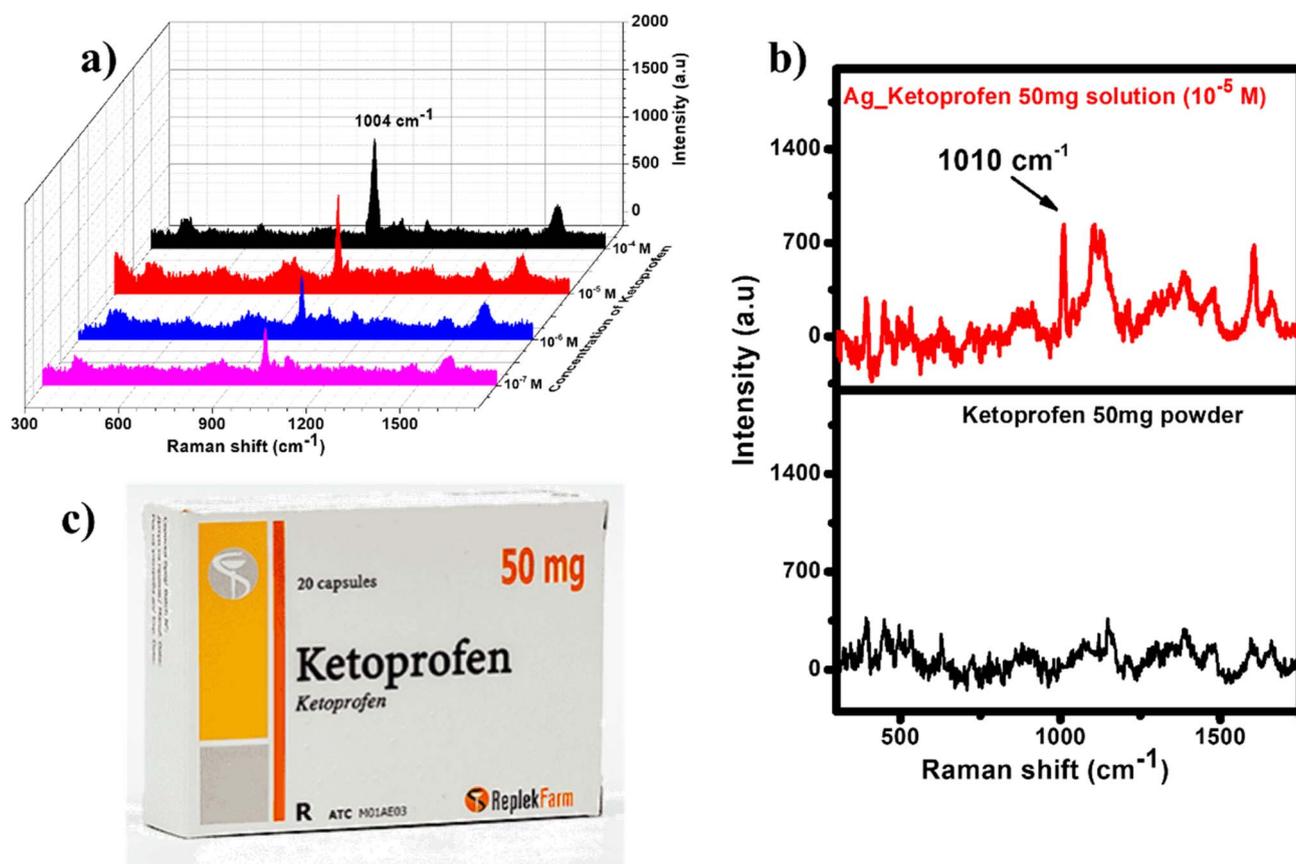

Fig. 10 (a) SERS spectra of TMP with different concentrations in tap water on the MnO_2-s/e-Ag SERS substrate; (b) Raman spectra of commercial KTP tablet solution, in which the concentration of KTP is approximately 10^{-5} M calculated based on establish TMP content, on e-AgNPs with (red) and without (black) e-AgNPs as SERS active substrates.; (c) commercial KTP.

band, the TMP concentration in the solution prepared as described in Section 2.4 was estimated to be 8.6×10^{-5} M, with a recovery of 86% compared to the labeled amount.

Similarly, KTP was spiked into tap water at concentrations from 10^{-4} M to 10^{-7} M for SERS measurements. Fig. 10a displays the SERS spectra of KTP at different concentrations on the e-AgNP substrate, exhibiting characteristic peaks at 704, 1004, 1031, 1138, 1194, and 1598 cm^{-1}. The intensities of these bands decreased consistently as the concentration was reduced from 10^{-4} M to 10^{-7} M. Quantitative recovery rates ranged from 88% to 95% (Table S2). In addition, the KTP content was determined in a commercial tablet (Fig. 10b). The SERS spectrum of the tablet displayed several additional bands attributed to excipients, but the dominant KTP peak remained clearly detectable. Based on this band, the TMP concentration in the solution prepared as described in Section 2.4 was estimated to be 9.0×10^{-6} M, with a recovery of 90% compared to the labeled amount.

4. Conclusions

This work demonstrates that although TMP and KTP exhibit similar frontier orbital energies, their SERS responses differ fundamentally due to adsorption-driven effects. TMP benefits from strong chemisorption *via* pyrimidine nitrogens, enabling direct and highly sensitive quantification with e-AgNP substrates. In contrast, KTP shows weak adsorption and poor intrinsic detectability, but chloride-mediated surface activation effectively overcomes this limitation by creating Ag–Cl$_x^-$ states and facilitating charge transfer. The resulting enhancement allows KTP to be quantified with sensitivity and reproducibility comparable to TMP. Validation in tap water and pharmaceutical tablets confirms that the sensors are reliable in complex matrices, with recoveries above 85%. These findings emphasize that adsorption geometry, not just energy-level alignment, governs SERS performance, and that interfacial chemistry can be engineered to expand the scope of SERS to more challenging analytes. More broadly, the findings underscore that adsorption geometry and surface interactions, alongside electronic alignment, govern SERS performance and that these parameters can be engineered to expand the range of analytes accessible to SERS.

Author contributions

D. T. N. Nga: conceptualization, methodology, investigation, formal analysis, writing-original draft; H. A. Nguyen: conceptualization, methodology, investigation, formal analysis, writing-original draft; M. Q. Doan: conceptualization, methodology, investigation; A. T. Le: conceptualization, methodology, supervision, project administration, writing-review & editing.

Conflicts of interest

The authors declare that they have no known competing financial interests or personal relationships that could have appeared to influence the work reported in this paper.

Data availability

All data supporting the findings of this study are available within the article and its supplementary information (SI). Supplementary information: calculation of detection limit and relative standard deviation; plot of the SERS intensity at 270 nm and 260 nm against TMP and KTP concentration in the standard solution; normalized adsorption spectra of e-AgNPs in glycerol (0–32%); plot of $\lambda_{\max}$ of the absorption spectra of e-AgNPs in glycerol (0–32%) *versus* n measured by refractometer; normalized adsorption spectra of e-AgNPs in the presence of TMP and KTP in comparison with that of pure e-AgNPs; SERS spectra of TMP (4×10^{-9} M) and KTP (5×10^{-8} M) on e-AgNPs; SERS spectra of TMP and KTP on freshly prepared and 4-week stored e-AgNPs; recovery values for four concentrations of TMP and KTP in the tap-water sample. See DOI: **https://doi.org/10.1039/d5ra07249b**.

References

1 J. Georgin, D. S. P. Franco, K. da Boit Martinello, E. C. Lima and L. F. O. Silva, *J. Environ. Chem. Eng.*, 2022, **10**, 107798.

2 B. Rangasamy, D. Hemalatha, C. Shobana, B. Nataraj and M. Ramesh, *Chemosphere*, 2018, **213**, 423–433.

3 E. Kortesmäki, J. R. Östman, A. Meierjohann, J. M. Brozinski, P. Eklund and L. Kronberg, *Environ. Toxicol. Chem.*, 2020, **39**, 1774–1789.

4 J. M. Balbus, A. B. A. Boxall, R. A. Fenske, T. E. McKone and L. Zeise, *Environ. Toxicol. Chem.*, 2013, **32**, 62–78.

5 C. Uluseker, K. M. Kaster, K. Thorsen, D. Basiry, S. Shobana, M. Jain, G. Kumar, R. Kommedal and I. Pala-Ozkok, *Front. Microbiol.*, 2021, **12**, 717809.

6 B. S. Diogo, S. Rodrigues, O. Golovko and S. C. Antunes, *Environ. Sci. Pollut. Res.*, 2024, **31**, 52233–52252.

7 N. Kraupner, S. Ebmeyer, M. Hutinel, J. Fick, C.-F. Flach and D. G. J. Larsson, *Environ. Int.*, 2020, **144**, 106083.

8 K. O'Malley, W. McDonald and P. McNamara, *Environ. Sci.: Water Res. Technol.*, 2023, **9**, 2188–2212.

9 Z. Lu, A. K. Mahony, W. A. Arnold, C. W. Marshall and P. J. McNamara, *Environ. Sci.: Adv.*, 2024, **3**, 208–226.

10 W. M. Kadoya, R. Sierra-Alvarez, B. Jagadish, S. Wong, L. Abrell, E. A. Mash and J. A. Field, *Chemosphere*, 2019, **222**, 789–796.

11 A. Kruve, R. Rebane, K. Kipper, M.-L. Oldekop, H. Evard, K. Herodes, P. Ravio and I. Leito, *Anal. Chim. Acta*, 2015, **870**, 29–44.

12 D. Steiner, A. Malachová, M. Sulyok and R. Krska, *Anal. Bioanal. Chem.*, 2021, **413**, 25–34.

13 P. A. Mosier-Boss, *Nanomaterials*, 2017, **7**, 142.

14 S. Schlücker, *Angew. Chem., Int. Ed.*, 2014, **53**, 4756–4795.

15 E. C. Le Ru and P. G. Etchegoin, in *Principles of Surface-Enhanced Raman Spectroscopy*, ed. E. C. Le Ru and P. G. Etchegoin, Elsevier, Amsterdam, 2009, pp. 185–264, DOI: 10.1016/B978-0-444-52779-0.00010-6.

16 J. R. Lombardi and R. L. Birke, *J. Phys. Chem. C*, 2008, **112**, 5605–5617.

17 J. N. Anker, W. P. Hall, O. Lyandres, N. C. Shah, J. Zhao and R. P. Van Duyne, *Nat. Mater.*, 2008, **7**, 442–453.

18 J. Yi, E.-M. You, R. Hu, D.-Y. Wu, G.-K. Liu, Z.-L. Yang, H. Zhang, Y. Gu, Y.-H. Wang, X. Wang, H. Ma, Y. Yang, J.-Y. Liu, F. R. Fan, C. Zhan, J.-H. Tian, Y. Qiao, H. Wang, S.-H. Luo, Z.-D. Meng, B.-W. Mao, J.-F. Li, B. Ren, J. Aizpurua, V. A. Apkarian, P. N. Bartlett, J. Baumberg, S. E. J. Bell, A. G. Brolo, L. E. Brus, J. Choo, L. Cui, V. Deckert, K. F. Domke, Z.-C. Dong, S. Duan, K. Faulds, R. Frontiera, N. Halas, C. Haynes, T. Itoh, J. Kneipp, K. Kneipp, E. C. Le Ru, Z.-P. Li, X. Y. Ling, J. Lipkowski, L. M. Liz-Marzán, J.-M. Nam, S. Nie, P. Nordlander, Y. Ozaki, R. Panneerselvam, J. Popp, A. E. Russell, S. Schlücker, Y. Tian, L. Tong, H. Xu, Y. Xu, L. Yang, J. Yao, J. Zhang, Y. Zhang, Y. Zhang, B. Zhao, R. Zenobi, G. C. Schatz, D. Graham and Z.-Q. Tian, *Chem. Soc. Rev.*, 2025, **54**, 1453–1551.

19 Y. Wu, S. Weng, T. Wang, K. V. Kong and D. Lin, *Anal. Methods*, 2025, **17**, 4482–4495.

20 Q. D. Mai, H. A. Nguyen, T. L. H. Phung, N. Xuan Dinh, Q. H. Tran, T. Q. Doan and A.-T. Le, *J. Phys. Chem. C*, 2022, **126**, 7778–7790.

21 M. Q. Doan, N. H. Anh, N. X. Quang, N. X. Dinh, D. Q. Tri, T. Q. Huy and A.-T. Le, *J. Electron. Mater.*, 2022, **51**, 150–162.

22 H. Bin, L. Gao, Z.-G. Zhang, Y. Yang, Y. Zhang, C. Zhang, S. Chen, L. Xue, C. Yang, M. Xiao and Y. Li, *Nat. Commun.*, 2016, **7**, 13651.

23 M. Bilal, T. Rasheed, H. M. N. Iqbal, C. Li, H. Hu and X. Zhang, *Int. J. Biol. Macromol.*, 2017, **105**, 393–400.

24 P. Mulvaney, *Langmuir*, 1996, **12**, 788–800.

25 M. Mayer, M. J. Schnepf, T. A. F. König and A. Fery, *Adv. Opt. Mater.*, 2019, **7**, 1800564.

26 M. Asif, R. Yasmin, R. Asif, A. Ambreen, M. Mustafa and S. Umbreen, *Dose-Response*, 2022, **20**, 15593258221088709.

27 S. Kenmotsu, M. Hirasawa, T. Tamadate, C. Matsumoto, S. Osone, Y. Inomata and T. Seto, *ACS Omega*, 2024, **9**, 37716–37723.

28 K. G. Stamplecoskie, J. C. Scaiano, V. S. Tiwari and H. Anis, *J. Phys. Chem. C*, 2011, **115**, 1403–1409.

29 P. G. Etchegoin and E. C. Le Ru, in *Surface Enhanced Raman Spectroscopy*, 2010, pp. 1–37, DOI: 10.1002/9783527632756.ch1.

30 K. A. Willets and R. P. Van Duyne, *Annu. Rev. Phys. Chem.*, 2007, **58**, 267–297.

31 Q. Sun, H. Wang, C. Yang and Y. Li, *J. Mater. Chem.*, 2003, **13**, 800–806.

32 H. Eckhardt, L. W. Shacklette, K. Y. Jen and R. L. Elsenbaumer, *J. Chem. Phys.*, 1989, **91**, 1303–1315.

33 A. Ungurean, N. Leopold, L. David and V. Chiș, *Spectrochim. Acta, Part A*, 2013, **102**, 52–58.

34 M. L. Vueba, M. E. Pina, F. Veiga, J. J. Sousa and L. A. E. B. de Carvalho, *Int. J. Pharm.*, 2006, **307**, 56–65.

35 K. Logacheva, P. Gergelezhiu, E. Raksha, L. Savostina, G. Arzumanyan, A. Eresko, S. Malakhov, K. Mamatkulov, O. Ponomareva, A. Belushkin and D. Chudoba, *Phys. Part. Nucl. Lett.*, 2024, **21**, 839–842.

36 M. Moskovits, *Rev. Mod. Phys.*, 1985, **57**, 783–826.

37 M. Moskovits, *J. Raman Spectrosc.*, 2005, **36**, 485–496.

38 L. Guerrini and D. Graham, *Chem. Soc. Rev.*, 2012, **41**, 7085–7107.

39 C. Hansch, A. Leo and R. W. Taft, *Chem. Rev.*, 1991, **91**, 165–195.

40 N. Ha Anh, M. Quan Doan, N. Xuan Dinh, T. Quang Huy, D. Quang Tri and A.-T. Le, *Appl. Surf. Sci.*, 2022, **584**, 152555.

41 D. Sajan, A. Fischer, I. H. Joe and V. S. Jayakumar, *Spectrochim. Acta, Part A*, 2006, **64**, 580–585.

42 N. Leopold, A. Stefancu, K. Herman, I. S. Tódor, S. D. Iancu, V. Moisoiu and L. F. Leopold, *Beilstein J. Nanotechnol.*, 2018, **9**, 2236–2247.

43 N. Leopold and B. Lendl, *J. Phys. Chem. B*, 2003, **107**, 5723–5727.

44 A. Otto, I. Mrozek, H. Grabhorn and W. Akemann, *J. Condens. Matter Phys.*, 1992, **4**, 1143.

45 P. Liu, R. Zhang, L. Zheng and Q. Cao, *Chemosensors*, 2023, **11**, 339.

46 M. H. A. Feitosa, A. M. Santos, A. Wong, R. S. Rocha and F. C. Moraes, *Analytica*, 2023, **4**, 159–169.

47 V. B. Patil, D. Ilager, S. M. Tuwar, K. Mondal and N. P. Shetti, *Bioengineering*, 2022, **9**, 521.

48 F. L. Soares, B. R. Junior and R. L. Carneiro, *Chemosensors*, 2022, **10**, 528.

49 J. P. Chu, Y.-J. Yeh, C.-Y. Liu, Y.-X. Yang, A. K. Altama, T.-H. Chang, W.-H. Chiang, P. Yiu and K.-L. Tung, *J. Vac. Sci. Technol., A*, 2023, **41**, 063111.

50 A. Obaid, A. K. Mohd Jamil, S. M. Saharin and S. Mohamad, *Chirality*, 2021, **33**, 810–823.

51 H. Le Thi Minh, L. Tran Thi, H. Kim Nhat, H. Nguyen Thi Anh, T. Dao Anh, T. Nguyen Huu, K. Nguyen Duy and H. Le Vu Tuan, *J. Mater. Sci.: Mater. Electron.*, 2023, **34**, 283.

52 N. E. Markina, A. V. Markin, K. Weber, J. Popp and D. Cialla-May, *Anal. Chim. Acta*, 2020, **1109**, 61–68.